

Cite this: *Dalton Trans.*, 2024, **53**,
12943

Dual-nodes bridged cobalt-modified Keggin-type polyoxometalate-based chains for highly efficient CO₂ photoconversion†

Xin-Lian Chen, Jie Wu, Ji-Lei Wang,  Xiao-Mei Liu,  Hua Mei* and Yan Xu *

The design of efficient catalysts for photocatalytic CO₂ conversion is of great importance for the sustainable development of society. Herein, three polyoxometalate (POM)-based crystalline materials were formulated prepared by substituting transition metals and adjusting solvent acidity with 2-(2-pyridyl) benzimidazole (pyim) as the light-trapping ligand, namely {[SiW₁₂O₄₀][Co(pyim)₂]₂·2C₂H₅OH (SiW₁₂Co₂), {[SiW₁₂O₄₀][Ni(pyim)₂]₂·2C₂H₅OH (SiW₁₂Ni₂), and {[SiW₁₂O₄₀][Mn(pyim)₂]₂·2C₂H₅OH (SiW₁₂Mn₂). X-ray crystallography diffraction analysis indicates that the three complexes exhibit isostructural properties, and form a stable one-dimensional chain structure stabilized by two [M(pyim)₂]₂²⁺ (M = Co, Ni, and Mn) fragments serving as dual-nodes to the adjacent SiW₁₂ units. A comprehensive analysis of the structural characterization and photocatalytic CO₂ reduction properties is presented. Under light irradiation, SiW₁₂Co₂ exhibited a remarkable CO generation rate of 10 733 μmol g⁻¹ h⁻¹ with a turnover number of 328, outperforming most of the reported heterogeneous POM-based photocatalysts. Besides, cycling tests revealed that SiW₁₂Co₂ is an efficient and stable photocatalyst with great recyclability for at least four successive runs. This study proves that the successful incorporation of diverse transition metals into the POM anion could facilitate the development of highly efficient photocatalysts for the CO₂RR.

Received 17th June 2024,
Accepted 11th July 2024

DOI: 10.1039/d4dt01757a

rsc.li/dalton

Introduction

The continued massive consumption of non-renewable fossil fuels and increasing level of industrialization have reached a significant level of unsustainable development in recent years, and a serious energy crisis has been triggered.^{1–4} Moreover, the large amount of CO₂ emissions has led to global climate change, such as the greenhouse effect.^{5–8} One of the most effective strategies to mitigate the greenhouse effect and bring about the carbon cycle is converting CO₂ into valuable products (CO, CH₄, etc.).^{9–15} Until now, the conversion of solar energy into chemical energy through photocatalytic reactions has been widely studied in numerous fields. Compared with traditional catalytic methods, the most promising approach for efficient and sustainable energy production and conversion is to transform atmospheric carbon dioxide into renewable energy substitutes.^{16–19} Currently, the solar-driven catalytic reduction of carbon dioxide to hydrocarbon fuels (*e.g.*, CO,

CH₄, C₂H₄, C₂H₆) or chemicals (*e.g.*, HCOOH, CH₃OH, CH₃COOH) is a crucial and environmentally friendly but challenging approach for carbon recovery.^{20–23} Hence, it is necessary to develop efficient and selective catalysts.

It is a truth universally acknowledged that polyoxometalates (POMs) possess exceptional redox capacity and well-defined structures. Also, the structural dimensions can be adjusted by changing the constituent elements and organic bridging components.^{24–30} Furthermore, multiple electrons and protons can be stored while also allowing for rapid photo-responsive charge transfer and reversible redox reactions. Along with providing rich redox electron pairs, transition metals (such as Co, Ni, Mn, etc.) serve as sites of catalysis. Furthermore, they can unite with lacunary POMs to generate an array of polyoxometalates replaced with transition metals. Thus, researchers are increasingly interested in POM-based inorganic-organic hybrid materials that combine POMs with metal ions and organic ligands, given that POMs contain a large number of oxygen atoms on their outer surface, which can coordinate with metal ions or organic units to generate novel compounds.^{31–37} Yao and co-workers synthesized the first POM in 2019 comprising a nuclear Co cluster that had effective photocatalytic activity for CO₂ reduction. The maximum values of TON and TOF exhibited were 10 492 and 0.29 s⁻¹, respectively.³⁸ In 2020, Zhang's group reported a significant tungsten-substituted TiO₂, which contributed to the

College of Chemical Engineering, State Key Laboratory of Materials-Oriented Chemical Engineering, Nanjing Tech University, Nanjing 211800, P. R. China.
E-mail: yanxu@njtech.edu.cn

† Electronic supplementary information (ESI) available: Synthesis, details of crystallographic data, structural figures, PXRD patterns, and IR spectra characterization. CCDC 2359927–2359929. For ESI and crystallographic data in CIF or other electronic format see DOI: <https://doi.org/10.1039/d4dt01757a>

generation of Ti vacancies that served as catalytically active sites for reducing CO₂.³⁹ Based on the above considerations, the objective was to enhance photocatalysis by incorporating Co, Ni, and Mn elements separately into tungsten-containing POMs to generate novel compounds.

In view of the aforementioned literature, we utilized 2-(2-pyridyl)benzimidazole (pyim) as an organic ligand, and {SiW₁₂O₄₀} as the molecular unit to construct new compounds with transition metal ions (Co, Ni, and Mn) to use as linkers in order to generate three novel Keggin-type {SiW₁₂O₄₀}-based 1D chains under hydrothermal conditions: {[SiW₁₂O₄₀][Co(pyim)₂]₂·2C₂H₅OH (SiW₁₂Co₂), {[SiW₁₂O₄₀][Ni(pyim)₂]₂·2C₂H₅OH (SiW₁₂Ni₂), and {[SiW₁₂O₄₀][Mn(pyim)₂]₂·2C₂H₅OH (SiW₁₂Mn₂). All three compounds are composed of {SiW₁₂O₄₀} units, transition metals, and ligands in a three-dimensional supramolecular structure. Notably, SiW₁₂Co₂ exhibits the highest catalytic activity in the photocatalytic CO₂RR. When 0.54 μmol of SiW₁₂Co₂ was introduced, the turnover numbers (TON) of CO and H₂ achieved the values of 328 and 181, respectively, where the yields were, respectively, 177.1 and 97.6 μmol, and the production rates were 10 733 and 6100 μmol g⁻¹ h⁻¹ under eight-hour irradiation periods. SiW₁₂Ni₂ has only weak photocatalytic CO₂RR activity, but it does provide a higher CO/H₂ ratio and optimum selectivity for CO (82.5%). Additionally, SiW₁₂Co₂ possesses excellent chemical stability, enabling it to maintain its structural integrity after four catalytic cycles.

Experimental section

Synthesis of compounds

{[SiW₁₂O₄₀][Co(pyim)₂]₂·2C₂H₅OH (SiW₁₂Co₂). A solution was prepared by dissolving the mixture of H₄[SiW₁₂O₄₀]-6H₂O (0.4480 g, 0.15 mmol), Co(OAc)₂·4H₂O (0.1245 g, 0.50 mmol), and pyim (0.0400 g, 0.20 mmol) in 12 mL of mixed solvent [(water):(ethanol) = 8:4 v/v] and stirring for 0.5 h at room temperature. Then, NaOH (1 M) was used to modulate the pH to approximately 3.0, and the resulting mixture was stirred for a further half hour. Subsequently, the aforementioned mixture was sealed within a Teflon-lined stainless-steel autoclave and maintained at 170 °C for a period of 3 days. Ultimately, once room temperature was reached, orange-red parallelogram block crystals were extracted using filtration and cleaned with distilled water. Yield: 45% (based on pyim). Found (%): C, 15.56; H, 1.12; N, 4.66; anal. calcd (%): C, 15.71; H, 1.10; N, 4.40. IR (KBr pellet, cm⁻¹): 3444 (m), 2931 (w), 1600 (m), 1439 (m), 1383 (s), 1012 (m), 924 (s), 796 (s) (Fig. S10a†).

{[SiW₁₂O₄₀][Ni(pyim)₂]₂·2C₂H₅OH (SiW₁₂Ni₂). The synthetic procedure of SiW₁₂Ni₂ is analogous to that of SiW₁₂Co₂, except that Co(OAc)₂·4H₂O (0.1245 g, 0.50 mmol) was substituted for Ni(OAc)₂·4H₂O (0.1244 g, 0.50 mmol). The solution pH was adjusted to about 3.0 with HCl (1 M). SiW₁₂Ni₂ exhibited yellow-green parallelogram block crystals. Yield: 42% (based on pyim). Found (%): C, 15.47; H, 1.07; N, 4.64; anal. calcd (%): C, 15.71; H, 1.10; N, 4.40. IR (KBr pellet, cm⁻¹): 3386 (m),

2918 (w), 1604 (m), 1442 (m), 1384 (s), 1012 (m), 924 (s), 799 (s) (Fig. S10b†).

{[SiW₁₂O₄₀][Mn(pyim)₂]₂·2C₂H₅OH (SiW₁₂Mn₂). The synthetic procedure of SiW₁₂Mn₂ is analogous to that of SiW₁₂Co₂, except that Co(OAc)₂·4H₂O (0.1245 g, 0.50 mmol) was replaced with Mn(OAc)₂·4H₂O (0.1225 g, 0.50 mmol). HCl (1 M) was added to the solution to adjust its pH to 3.5. Orange parallelogram block crystals were eventually produced. Yield: 34% (based on pyim). Found (%): C, 15.50; H, 1.07; N, 4.70; anal. calcd (%): C, 15.74; H, 1.10; N, 4.44. IR (KBr pellet, cm⁻¹): 3378 (m), 2925 (w), 1601 (m), 1439 (m), 1442 (s), 1016 (m), 923 (s), 806 (s) (Fig. S10c†).

Results and discussion

Crystal structure

X-ray diffraction crystallography analysis indicated that these three compounds exhibit semblable primary structures where only the transition metals present differences, and that they all crystallize in the triclinic system with a *P* $\bar{1}$ space group (Table 1). The surface morphology of the crystals of SiW₁₂M₂ (M = Co, Ni, and Mn) has been clearly visualized under an optical microscope (Fig. S1†) and mapped by scanning electron microscopy (Fig. S14–S16†). Since the three compounds are isostructural, only SiW₁₂Co₂ is exemplified here for a better understanding of its structure. There are basically two components that comprise the compounds: [SiW₁₂O₄₀]⁴⁻ and [Co(pyim)₂]²⁺ (Fig. 1a and b). The asymmetric unit of the compounds comprises half of one {SiW₁₂O₄₀} node, two transition metal ions, four pyim ligands, as well as two free ethanol molecules (Fig. S2 and S6†). There is only one kind of metal-coordinated environment in the Co cluster. Each Co atom is connected to two pyim ligands (Fig. 1a). In concrete terms, two Co ions are both in a hexacoordinated environment, with 4 N atoms from 2 pyim ligands and 2 O atoms from two adjacent {SiW₁₂O₄₀} units, with the unit exhibiting a common distorted octahedral geometry (Fig. S3 and S6b†). Also, there exists only one type of coordination environment for pyim in the structure. The ball-shaped cluster {SiW₁₂O₄₀} is widely perceived as a heteroatomic α -Keggin POM with twelve tungsten atoms surrounding the central silicon atom with an approximate size of 10.4 Å × 10.4 Å (Fig. 1b). Twelve tungsten ions are distributed in three layers from top to bottom in a “3 + 6 + 3” arrangement. The {SiW₁₂O₄₀} node can be viewed as a four-connected linkage to coordinate four Co ions by W–O–Co bonds (Fig. S6a†). Two adjacent POM units are connected to each other by two transition metal complex units, generating an infinite 1D chain-like structure (Fig. 1c). Moreover, Fig. 1d shows the simplified structure of a one-dimensional chain, in which purple balls represent the [Co(pyim)₂]₂²⁺ fragments while yellow balls denote the Keggin POM. Two adjacent POMs in 1D chains form dual-nodes through two [Co(pyim)₂]₂²⁺ fragments. Compared with most polyoxometalate compounds, a common prominent structural feature of these three compounds is the dual nodes of transition metals, which make their structures more stable than typical structures.^{40,41,58}

Table 1 Crystallographic information for the three compounds

| Complexes | SiW₁₂Co₂ | SiW₁₂Ni₂ | SiW₁₂Mn₂ |
|---|---|---|---|
| Formula | C ₅₂ H ₄₈ N ₁₂ Co ₂ O ₄₂ SiW ₁₂ | C ₅₂ H ₄₈ N ₁₂ Ni ₂ O ₄₂ SiW ₁₂ | C ₅₂ H ₄₈ N ₁₂ Mn ₂ O ₄₂ SiW ₁₂ |
| Formula weight | 3865.17 | 3864.73 | 3857.19 |
| T (K) | 293(2) | 293(2) | 293(2) |
| Crystal system | Triclinic | Triclinic | Triclinic |
| Space group | <i>P</i> $\bar{1}$ | <i>P</i> $\bar{1}$ | <i>P</i> $\bar{1}$ |
| <i>a</i> (Å) | 11.981(9) | 11.9589(16) | 11.974(8) |
| <i>b</i> (Å) | 12.240(9) | 12.1998(16) | 12.380(8) |
| <i>c</i> (Å) | 14.091(11) | 14.0482(19) | 14.074(9) |
| α (°) | 101.102(9) | 101.336(2) | 101.321(8) |
| β (°) | 98.930(10) | 98.179(2) | 98.243(8) |
| γ (°) | 108.668(9) | 108.916(2) | 108.981(7) |
| <i>V</i> (Å ³) | 1868(2) | 1853.6(4) | 1886(2) |
| <i>Z</i> | 1 | 1 | 1 |
| <i>D_c</i> (mg m ⁻³) | 3.436 | 3.462 | 3.397 |
| μ (mm ⁻¹) | 18.937 | 19.145 | 18.656 |
| <i>F</i> (000) | 1736 | 1738 | 1732 |
| θ range (°) | 1.515–25.010 | 1.516–25.006 | 1.514–25.009 |
| Crystal size (mm ³) | 0.13 × 0.12 × 0.11 | 0.13 × 0.12 × 0.11 | 0.13 × 0.12 × 0.11 |
| Limiting indices | −13 ≤ <i>h</i> ≤ 14, −14 ≤ <i>k</i> ≤ 14, −16 ≤ <i>l</i> ≤ 16 | −14 ≤ <i>h</i> ≤ 14, −14 ≤ <i>k</i> ≤ 13, −16 ≤ <i>l</i> ≤ 16 | −14 ≤ <i>h</i> ≤ 14, −14 ≤ <i>k</i> ≤ 14, −16 ≤ <i>l</i> ≤ 14 |
| Reflections collected | 13 284 | 13 205 | 13 205 |
| <i>R</i> (int) | 0.0877 | 0.0670 | 0.0591 |
| Data/restraints/parameters | 6532/207/567 | 6455/233/567 | 6578/222/567 |
| GOF | 1.202 | 1.171 | 1.181 |
| <i>R</i> ₁ ^a , <i>wR</i> ₂ ^b [<i>I</i> > 2σ(<i>I</i>)] | <i>R</i> ₁ = 0.0729, <i>wR</i> ₂ = 0.1748 | <i>R</i> ₁ = 0.0687, <i>wR</i> ₂ = 0.1956 | <i>R</i> ₁ = 0.0648, <i>wR</i> ₂ = 0.1541 |
| <i>R</i> ₁ , <i>wR</i> ₂ (all data) | <i>R</i> ₁ = 0.0827, <i>wR</i> ₂ = 0.1788 | <i>R</i> ₁ = 0.0778, <i>wR</i> ₂ = 0.1998 | <i>R</i> ₁ = 0.0687, <i>wR</i> ₂ = 0.1559 |

$$^a R_1 = \sum ||F_o| - |F_c|| / \sum |F_o|. \quad ^b wR_2 = \sqrt{\sum [w(F_o^2 - F_c^2)^2] / \sum [w(F_o^2)^2]^{1/2}}.$$

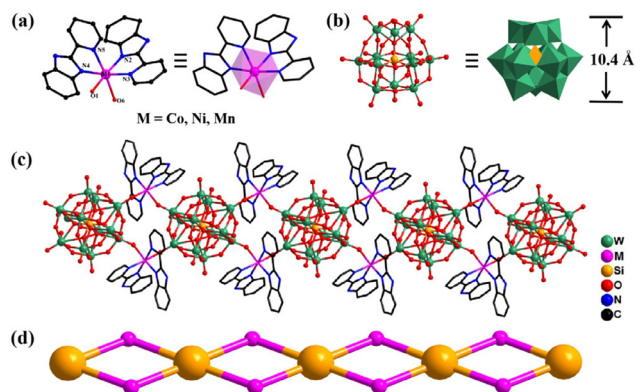


Fig. 1 The structure of SiW₁₂M₂ (M = Co, Ni, Mn): (a) the coordinating surroundings of the M node; (b) structure of the {SiW₁₂O₄₀} node; (c and d) 1D chain composed of M and {SiW₁₂O₄₀} and the simplified structure of the 1D chain.

In addition, adjacent 1D chains are arranged regularly to shape 2D supramolecular layers through π - π stacking interactions between pyim ligands, while the distance between layers is 9.2 Å (Fig. 2a, and S7[†]), and adjacent 2D supramolecular layers further contribute to the formation of the 3D supramolecular structure shown in Fig. 2b, facilitated by weak π - π stacking interactions between them. Based on bond valence sum (BVS) calculations, the valence states of M^{II} in these compounds were ascertained. The Co-O/N bonds range between 2.065(7) and 2.193(15) Å, all within the normal range of M^{II} compounds reported in the literature.⁴²

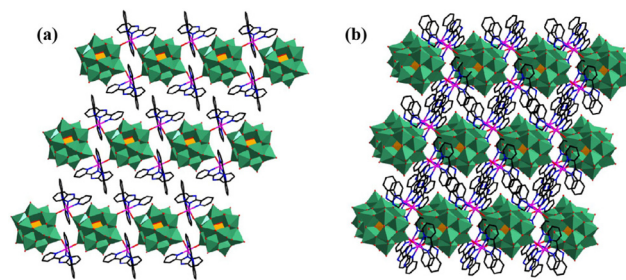


Fig. 2 (a) The 2D stacking diagram of SiW₁₂Co₂; (b) the 3D supramolecular framework of SiW₁₂Co₂.

Characterization

The PXRD patterns of these three compounds were first recorded at room temperature. The experimental results of the three samples can be well matched with the simulated patterns, proving the high phase purity of samples. Additionally, these compounds exhibit comparable diffraction peaks (Fig. S9[†]), demonstrating that they are isomorphous compounds. The conclusion is compatible with the results obtained from the resolution of the single-crystal structure. Subsequently, infrared (IR) spectra were produced to confirm the coordinated environment. As depicted in Fig. S10,[†] the IR spectra of these three isostructural compounds are analogous. Thus, analyzing the spectrum only for SiW₁₂Co₂ as an example, the broad peak at 3444 cm⁻¹ is assigned to the O-H stretching vibration; the peaks near 1012 and 924 cm⁻¹ are identified as being the characteristic signals of Si-O and

W=O, respectively, while the W–O–W vibration of the polyacid SiW₁₂ unit is observed at around 796 cm⁻¹. Furthermore, the peak at 2931 cm⁻¹ indicates the antisymmetric and symmetric stretching vibration of C–H, while the peaks in the range of 1600–1383 cm⁻¹ are stretching vibration signals for C=N, C=C, and C–N (Fig. S9a†). The results reveal successful ligand insertion with a coordination bond.

As effective absorption of sunlight is a prerequisite to photocatalysis, the light absorption range of these catalysts was characterized with UV-vis absorption spectroscopy. Taking SiW₁₂Co₂ as an example, the SiW₁₂ unit only absorbs in the UV range, whereas Co(OAc)₂ absorbs in the visible region (Fig. S11†), demonstrating that the absorption range of SiW₁₂Co₂ can be expanded by doping transition metals into the POMs up to a maximum absorption edge of 700 nm (Fig. 3a). The band gap energy of SiW₁₂Co₂ was further determined to be 2.55 eV *via* the Tauc plot (Fig. 3b), indicating that it has semiconductor-like characteristics. The energy is lower than that of the SiW₁₂ unit, which is 3.15 eV (Fig. S12c†), implying that it has both structural stability and potentially photocatalytic capability in CO₂RR catalytic systems.

Furthermore, to precisely ascertain electronic band locations, Mott–Schottky (MS) plot measurements were conducted at different frequencies: 2000 Hz, 2500 Hz, and 3000 Hz. The LUMO energy value was found to be -0.85 V (Fig. 3c). This sufficiently negative LUMO level demonstrated that the compound was able to turn CO₂ into CO, CH₄, *etc.* According to the results of the bandgap and MS plot, the band structure diagram of SiW₁₂Co₂ was obtained (Fig. 3d). In comparison with the normal hydrogen electrode (NHE), the conduction band (CB) position of SiW₁₂Co₂ is -0.85 V, which is below the reduction potential required for CO generation (CO₂/CO = -0.53 V *vs.* NHE), which indicates that SiW₁₂Co₂ would be able to catalyze the CO₂ photosynthetic reaction in theory.^{43–47}

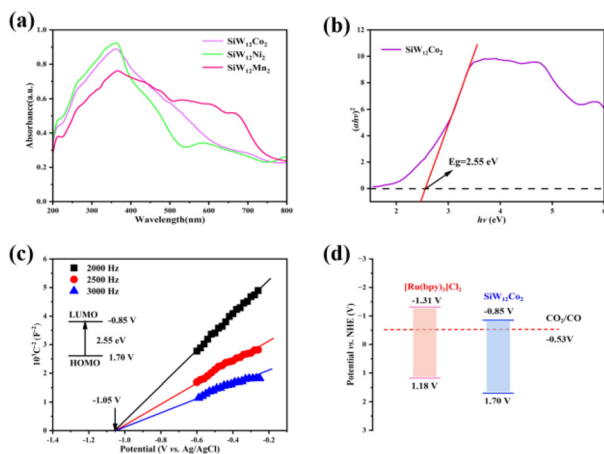


Fig. 3 (a) The UV-vis spectra of the three compounds; (b) band gap energy (E_g) analysis of SiW₁₂Co₂; (c) Mott–Schottky plots for SiW₁₂Co₂; (d) band-structure diagrams of SiW₁₂Co₂.

Photocatalytic CO₂ reduction

In accordance with the aforementioned UV-vis, Mott–Schottky, and energy band analysis, we utilized these SiW₁₂M₂ crystalline materials as photocatalysts for photocatalytic CO₂ reduction reactions (CO₂RR) in a CH₃CN solvent system containing the sacrificial reagent triethanolamine (TEOA) and photosensitizer [Ru(bpy)₃]Cl₂·6H₂O under a pure atmosphere of CO₂ (1.0 atm, 6 °C). All CO₂RRs were conducted in a thorough inquiry of the gas–liquid–solid system under visible light conditions ($\lambda = 420$ –800 nm). First, the three catalysts were used as photocatalysts, respectively, where the production of H₂, CO, and CH₄ was detected, although the trace yield of methane is not reflected in the figures. As illustrated in Fig. 4a, we employed the identical molar amount (2.7 μ mol) of catalyst and observed that the photocatalytic activity of SiW₁₂Co₂ exhibited a notably greater performance than SiW₁₂Ni₂ and SiW₁₂Mn₂ in the CO₂RR. The main products of the reaction were CO (278.1 μ mol) and H₂ (222.2 μ mol). The growth trend of CO increased linearly in an approximate time-dependent manner, demonstrating the relative stability of the photoreduction process within the initial 8 h (Fig. 4d). On comparing with SiW₁₂Co₂, SiW₁₂Ni₂ presents only weak photocatalytic CO₂RR activity, but it does provide a superior CO/H₂ ratio and optimum selectivity for CO (82.5%), which can be

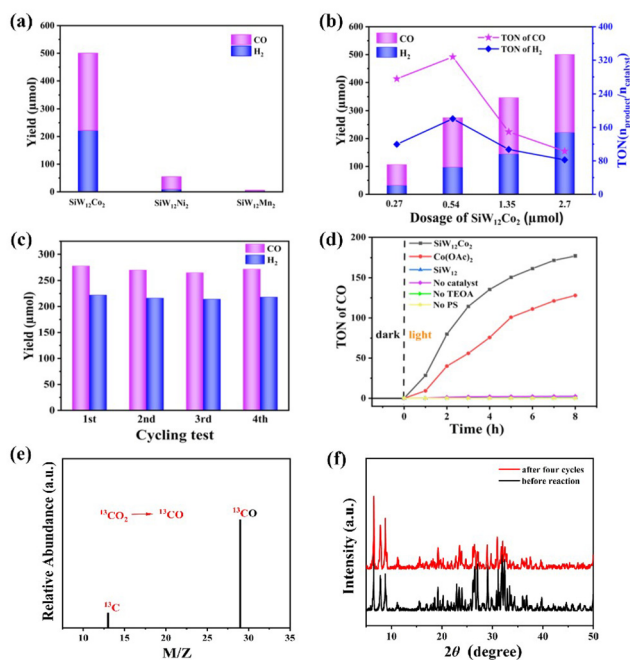


Fig. 4 (a) Comparison of the CO and H₂ yields in the photocatalytic system with SiW₁₂M₂ as catalysts. (b) The impact of various SiW₁₂Co₂ amounts on the yields of CO and H₂ (left axis) and the TON (right axis). (c) The change of CO and H₂ production when SiW₁₂Co₂ was used as catalyst after each cycle. (d) Comparison of the TON values under different photocatalysts. (e) The mass spectrum of ¹³CO ($m/z = 29$) generated by SiW₁₂Co₂. (f) The XRD patterns of SiW₁₂Co₂ before the reaction and after four reaction cycles. Reaction conditions: [Ru(bpy)₃]Cl₂·6H₂O (0.015 mmol), mixed solvents (50 mL, MeCN/TEOA, 4/1 v/v).

related to the higher capability of the Ni site to bind with high affinity. With regard to $\text{SiW}_{12}\text{Mn}_2$, only trace amounts of CO and H_2 are produced under identical reaction conditions.

In consideration of the higher catalytic activity of $\text{SiW}_{12}\text{Co}_2$, the effect of $\text{SiW}_{12}\text{Co}_2$ dosage on the CO_2RR was further assessed. As clarified in Fig. 4b, the amounts of CO and H_2 are raised as the quantity of $\text{SiW}_{12}\text{Co}_2$ is increased. With the addition of more catalyst (1.35, 2.7 μmol), the TON values of CO and H_2 were dramatically reduced. When 0.54 μmol of $\text{SiW}_{12}\text{Co}_2$ was introduced, the turnover numbers (TON) of CO and H_2 achieved their highest values of 328 and 181, respectively, which are higher than those reported for most nonhomogeneous POM-based photocatalysts (Table S4[†]). Additionally, the yields were 177.1 and 97.6 μmol along with product rates that were 10 733 and 6100 $\mu\text{mol g}^{-1} \text{h}^{-1}$ under eight-hour visible-light irradiation, respectively.

In addition, a succession of deletional comparative experiments with $\text{SiW}_{12}\text{Co}_2$ were carried out to assess the different influence of each component of the photocatalytic reaction conditions. The results are displayed in Fig. 4d and Table 2. A control experiment in the absence of $\text{SiW}_{12}\text{Co}_2$ showed that only trace amounts of products were generated, indicating that $\text{SiW}_{12}\text{Co}_2$ is indeed significantly important for the photocatalytic reaction (entry 4). Nothing was detected under dark reaction conditions, indicating that the reaction was a light-driven catalytic reaction (entry 5). Moreover, in the absence of $[\text{Ru}(\text{bpy})_3]\text{Cl}_2 \cdot 6\text{H}_2\text{O}$ or TEOA, gaseous or liquid products were hardly detected, suggesting that photosensitizers and sacrificial agents were critical for these photocatalysts in facilitating overall CO_2 reduction (entries 6 and 7). When exchanging CO_2 for Ar, only H_2 was detected, with no detectable levels of CO or CH_4 , manifesting that CO_2 was the sole contributor of carbon (entry 8). Noteworthy, when separately using equimolar amounts of the SiW_{12} unit and $\text{Co}(\text{OAc})_2$ instead of $\text{SiW}_{12}\text{Co}_2$ under the same reaction conditions, the SiW_{12} showed hardly any catalytic activity, whereas $\text{Co}(\text{OAc})_2$ exhibited average catalytic levels (CO, 128.0 μmol , H_2 , 58.1 μmol), manifesting that the Co ion in $\text{SiW}_{12}\text{Co}_2$ would be the main active center in CO_2

photoreduction (entries 2 and 3). In an effort to ensure the contribution of carbon over resultant gases, isotope studies were also conducted using $^{13}\text{CO}_2$ as a substrate under photocatalytic reaction conditions. The peak $m/z = 29$, as seen in Fig. 4e, is identified as ^{13}CO , revealing that $\text{SiW}_{12}\text{Co}_2$ is in fact able to effectively reduce CO_2 . The results of the above comparative experiments demonstrate that $[\text{Ru}(\text{bpy})_3]\text{Cl}_2 \cdot 6\text{H}_2\text{O}$, TEOA, and $\text{SiW}_{12}\text{Co}_2$ are indispensable in the photocatalytic CO_2 reduction system.

As stability and recoverability are vital indicators for evaluating the performance of photocatalysts, $\text{SiW}_{12}\text{Co}_2$ was used as an example for detailed evaluation owing to its excellent CO_2RR activity. $\text{SiW}_{12}\text{Co}_2$ was immersed in a mixed solvent (MeCN:TEOA = 4:1 v/v, 50 mL) as well as aqueous solutions of strong acid (pH = 2) and strong alkali (pH = 13), and no obvious color change of solutions was observed for 24 h (Fig. S20[†]). According to the PXRD patterns, $\text{SiW}_{12}\text{Co}_2$ possesses superb acid–base solvent stability, enabling it to maintain its crystalline integrity throughout the photocatalytic process owing to the stabilized 1D chain structure (Fig. S5, and S18[†]). Subsequently, photocatalytic cycling tests were conducted to investigate the recyclability of $\text{SiW}_{12}\text{Co}_2$ in the CO_2RR . Considering the loss of catalyst during the recycling process, the dosage was enhanced to 2.7 μmol instead of the optimal dosage (0.54 μmol). $\text{SiW}_{12}\text{Co}_2$ retains the great bulk of its original activity after four reaction cycles (Fig. 4c), demonstrating that $\text{SiW}_{12}\text{Co}_2$ possesses good photocatalytic stability. Besides, the PXRD pattern and IR spectra after the cycling experiments can well match those of prepared samples (Fig. 4f, and S18[†]), proving that the structure of $\text{SiW}_{12}\text{Co}_2$ maintains satisfactory stability in the photocatalytic process.

Mechanism

To fully comprehend the process of photo-excited electron migration, a photoluminescence (PL) quenching experiment was performed and time-resolved fluorescence decay spectra (TRPL) were recorded in the acetonitrile solutions containing photosensitizer (PS) and $\text{SiW}_{12}\text{Co}_2$, or electron sacrificial agents, with the solution concentration being proportional to that used for the photocatalytic reaction. As depicted in Fig. 5, the fluorescence intensity of the excited $[\text{Ru}(\text{bpy})_3]^{2+*}$ exhibits a gradual decline with augmentation of $\text{SiW}_{12}\text{Co}_2$, which is attributed to the attraction of the phosphorescence quenching of excited $[\text{Ru}(\text{bpy})_3]^{2+*}$ by continuous electron transfer to $\text{SiW}_{12}\text{Co}_2$ (Fig. 5b).⁴⁸ In addition, there is almost barely any change in the fluorescence spectra with varying concentrations of TEOA (Fig. 5a). TRPL spectra revealed that the excited luminescence of $[\text{Ru}(\text{bpy})_3]^{2+}$ conformed to single-exponential decay kinetics with respect to $\text{SiW}_{12}\text{Co}_2$ or TEOA. The lifetimes were designated by values of 384.88 ns and 436.63 ns, which reflect shorter lifespans than that of the separately existing $[\text{Ru}(\text{bpy})_3]^{2+}$ (469.41 ns) (Fig. 5d). The shortened lifespan indicates that the luminescence of photosensitizers added to an acetonitrile solution containing $\text{SiW}_{12}\text{Co}_2$ could decay more rapidly, validating that the electron transfer from photosensitizers to

Table 2 Comparison of the yield of product under different photocatalysts and reaction conditions

| Entry | Catalysts | Dosage (μmol) | CO (μmol) | H_2 (μmol) | CH_4 (μmol) | Notes |
|----------------|------------------------------|----------------------------|------------------------|----------------------------------|-----------------------------------|---------|
| 1 ^a | $\text{SiW}_{12}\text{Co}_2$ | 0.54 | 177.1 | 97.6 | 1.31 | Hetero. |
| 2 ^b | SiW_{12} | 0.54 | 0.59 | 21.2 | 0.34 | Homo. |
| 3 ^c | $\text{Co}(\text{OAc})_2$ | 1.08 | 128.0 | 58.1 | 1.61 | Homo. |
| 4 ^d | No catalysts | — | 2.52 | 3.63 | 0.68 | Homo. |
| 5 ^e | $\text{SiW}_{12}\text{Co}_2$ | 0.54 | — | — | — | Hetero. |
| 6 ^f | $\text{SiW}_{12}\text{Co}_2$ | 0.54 | 0.04 | — | 0.31 | Hetero. |
| 7 ^g | $\text{SiW}_{12}\text{Co}_2$ | 0.54 | 0.14 | — | 0.48 | Hetero. |
| 8 ^h | $\text{SiW}_{12}\text{Co}_2$ | 0.54 | — | 102.0 | — | Hetero. |

^a Reaction conditions: $\text{SiW}_{12}\text{Co}_2$ (0.54 μmol), $[\text{Ru}(\text{bpy})_3]\text{Cl}_2 \cdot 6\text{H}_2\text{O}$ (0.015 mmol), mixed solvents (50 mL, MeCN/TEOA, 4/1 v/v), CO_2 (1 atm), $\lambda = 420\text{--}800 \text{ nm}$, 6 $^\circ\text{C}$, 8 h, $5.2 \times 10^5 \text{ cd}$. ^b SiW_{12} replaced $\text{SiW}_{12}\text{Co}_2$. ^c $\text{Co}(\text{OAc})_2$ instead of $\text{SiW}_{12}\text{Co}_2$. ^d No catalyst. ^e Dark conditions. ^f No $[\text{Ru}(\text{bpy})_3]\text{Cl}_2 \cdot 6\text{H}_2\text{O}$. ^g No TEOA. ^h Ar instead of CO_2 .

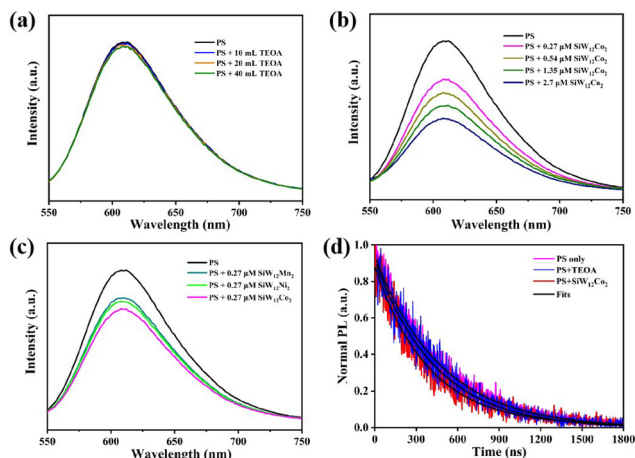


Fig. 5 Emission spectra of [Ru(bpy)₃]Cl₂ in different amounts of (a) TEOA ($\lambda_{\text{excitation}} = 510$ nm) and (b) SiW₁₂Co₂. (c) [Ru(bpy)₃]Cl₂ in MeCN solutions containing the catalysts SiW₁₂Co₂, SiW₁₂Ni₂ and SiW₁₂Mn₂; (d) time-resolved photoluminescence (TRPL) spectra of [Ru(bpy)₃]²⁺ and TEOA with the addition of SiW₁₂Co₂.

SiW₁₂Co₂ may lead to the phosphorescence quenching of photosensitizers. Compared to TEOA, SiW₁₂Co₂ promotes the separation of electron-hole pairs and suppresses their recombination more efficiently.⁴⁹ The results above suggest that the rate of the oxidation process of SiW₁₂Co₂ may be the decisive step of the reaction. Additionally, [Ru(bpy)₃]²⁺ is immediately quenched by SiW₁₂Co₂ rather than TEOA, indicating that the initial step of the photocatalytic CO₂RR primarily involves the transfer of electrons from the excited state of the PS to SiW₁₂Co₂ rather than from the TEOA.⁵⁰ Notably, in contrast to SiW₁₂Ni₂ and SiW₁₂Mn₂, the addition of SiW₁₂Co₂ significantly attenuates the PL intensity (Fig. 5c), which proves that the photo-induced electron transfer from [Ru(bpy)₃]²⁺ to SiW₁₂Co₂ is more efficient and effectively inhibits the quick recombination of holes and electrons on [Ru(bpy)₃]²⁺, and their fluorescence quenching ability was in accordance with the aforementioned photocatalytic CO₂RR.^{51,52}

The preceding results and discussions have led to the formulation of a possible reaction mechanism and electron transfer pathway for the photocatalytic CO₂ reduction by SiW₁₂Co₂ (Fig. 6). Under visible light irradiation, the photosensitizer [Ru(bpy)₃]Cl₂ is motivated to reach its excited state, subsequently undergoing an oxidative quenching process by SiW₁₂Co₂, resulting in the formation of the [Ru(bpy)₃]³⁺ oxidation state. The photogenerated electrons (e⁻) in [Ru(bpy)₃]Cl₂ leap from the HOMO energy to the LUMO energy level, creating a positively charged hole (h⁺) at the HOMO level. The photogenerated electrons spontaneously migrate from [Ru(bpy)₃]Cl₂ to the surface of SiW₁₂Co₂ by virtue of the positional matching of the LUMO energy levels between [Ru(bpy)₃]Cl₂ and SiW₁₂Co₂.⁵³ Remarkably, the presence of Co ions in SiW₁₂Co₂ plays a significant role in photocatalytic CO₂ reduction, as they enable the generation of ample numbers of high-energy electrons from the SiW₁₂ unit.¹⁴ Ultimately, TEOA serves as a sacrificial

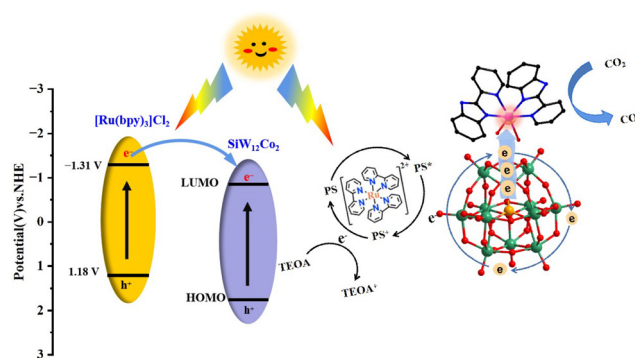


Fig. 6 Schematic diagram of electron transfer energy levels showing the proposed mechanism for photocatalytic CO₂ reduction over SiW₁₂Co₂.

electron donor, consuming the photogenerated holes formed in the [Ru(bpy)₃]²⁺ valence band, while the oxidized [Ru(bpy)₃]²⁺ is reduced to the original state [Ru(bpy)₃]³⁺. Simultaneously, TEOA is oxidized to TEOA⁺, which effectively prevents hole-electron recombination.^{54–58}

Conclusions

In general, we have successfully designed and synthesized three isostructural α -Keggin-type POM-based organic-inorganic metal 1D chains (SiW₁₂Co₂, SiW₁₂Ni₂, SiW₁₂Mn₂). Specifically, two adjacent SiW₁₂ units are connected *via* dual [M(pyim)₂]²⁺ fragments, resulting in the formation of a fairly stable 1D chain with dual nodes. Based on the above UV-vis, Mott-Schottky, and energy band analyses, these three compounds can be used as CO₂RR photocatalysts. Under light irradiation, SiW₁₂Co₂ possesses superior photocatalytic capability to that of both SiW₁₂Ni₂ and SiW₁₂Mn₂. In concrete terms, the optimal dosage of SiW₁₂Co₂ was found to be 0.54 μmol with a formation rate of 10 733 $\mu\text{mol g}^{-1} \text{h}^{-1}$, while the turnover number of CO reached 328 during an eight-hour photocatalysis period. Furthermore, SiW₁₂Co₂ can maintain better activity throughout four reaction cycles. Also, we investigated the electron transfer pathway in the photocatalytic CO₂RR using fluorescence emission spectra and proposed a possible reaction mechanism. The quenching mechanism can help us to better understand the discrepancy in the CO₂RR activities of POM-based compounds modified with different transition metals.

Author contributions

Xin-Lian Chen: writing of the original draft. Jie Wu: review and editing of the manuscript. Ji-Lei Wang: review and editing of the manuscript. Xiao-Mei Liu: review and editing of the manuscript. Hua Mei: writing, review and editing of the manuscript. Yan Xu: formal analysis, writing, review and editing of the manuscript.

Data availability

The authors confirm that the data supporting the findings of this study are available within the article and ESI.†

Conflicts of interest

The authors proclaim no competing financial conflicts.

Acknowledgements

This work was supported by the National Natural Science Foundation of China (92161109), the Postgraduate Research & Practice Innovation Program of Jiangsu Province (SJCX23_0451), and the Cultivation Program for The Excellent Doctoral Dissertation of Nanjing Tech University (2023-10).

References

- G. V. Last and M. T. Schmick, *Environ. Earth Sci.*, 2015, **74**, 1189–1198.
- D. C. N. Gruber, B. R. Carter, R. A. Feely, S. Heuven, M. Hoppema, M. Ishii, R. M. Key, A. Kozyr, S. K. Lauvset, C. L. Monaco, J. T. Mathis, A. O. A. Murata, F. F. Perez, C. L. Sabine, T. Tanhua and R. Wanninkhof, *Science*, 2019, **363**, 1193–1199.
- C. Steinlechner and H. Junge, *Angew. Chem., Int. Ed.*, 2018, **57**, 44–45.
- X. X. Li, L. Zhang, L. Yuan, T. Wang, L. Z. Dong, K. Huang, J. Liu and Y. Q. Lan, *Chem. Eng. J.*, 2022, **442**, 136157.
- S. C. Blanco, H. Zhang, J. M. Kim, Y. X. Shen and P. D. Yang, *Nat. Catal.*, 2020, **3**, 245–255.
- S. R. Nicholson, N. A. Rorrer, A. C. Carpenter and G. T. Beckham, *Joule*, 2021, **5**, 673–686.
- M. Lu, M. Zhang, J. Liu, T. Y. Yu, J. N. Chang, L. J. Shang, S. L. Li and Y. Q. Lan, *J. Am. Chem. Soc.*, 2022, **144**, 1861–1871.
- D. Shindell and C. J. Smith, *Nature*, 2019, **573**, 408–411.
- Y. R. Li, S. T. Li and H. W. Huang, *Chem. Eng. J.*, 2023, **457**, 141179.
- J. Liang, H. Yu, J. J. Shi, B. Li, L. X. Wu and M. Wang, *Adv. Mater.*, 2023, **35**, 2209814.
- W. H. Zhang, A. R. Mohamed and W. J. Ong, *Angew. Chem., Int. Ed.*, 2020, **59**, 22894–22915.
- Y. F. Mu, C. Zhang, M. R. Zhang, W. Zhang, M. Zhang and T. B. Lu, *ACS Appl. Mater. Interfaces*, 2021, **13**, 22314–22322.
- B. Obama, *Science*, 2017, **355**, 6321.
- S. H. Guo, X. J. Qi, H. M. Zhou, J. Zhou, X. H. Wang, M. Dong, X. Zhao, C. Y. Sun, X. L. Wang and Z. M. Su, *J. Mater. Chem. A*, 2020, **8**, 11712–11718.
- X. Y. Xiang, J. L. Zhou, Q. Wang, Y. H. Zhu, Z. T. Zhang, T. C. Ye, J. L. Wang, Q. L. Chen and Y. Xu, *Inorg. Chem.*, 2023, **62**, 5200–5206.
- C. Wang, C. Y. Zhu, M. Zhang, Y. Geng, Y. G. Li and Z. M. Su, *J. Mater. Chem. A*, 2020, **8**, 14807–14814.
- J. W. Fu, K. X. Jiang, X. Q. Qiu, J. G. Yu and M. Liu, *Mater. Today*, 2020, **32**, 222–243.
- Y. J. Gao, L. Zhang, Y. M. Gu, W. W. Zhang, Y. Pan, W. H. Fang, J. Ma, Y. Q. Lan and J. Bai, *Chem. Sci.*, 2020, **11**, 10143–10148.
- Y. Bai, P. Yang, L. Wang, B. Yang, H. Q. Xie, Y. Zhou and L. Q. Ye, *Chem. Eng. J.*, 2019, **360**, 473–482.
- Y. Z. Zhu, C. Gao, S. Bai, S. M. Chen, R. Long, L. Song, Z. Q. Li and Y. J. Xiong, *Nano Res.*, 2017, **10**, 3396–3406.
- X. X. Li, J. Liu, L. Zhang, L. Z. Dong, Z. F. Xin, S. L. Li, X. Q. Huang Fu, K. Huang and Y. Q. Lan, *ACS Appl. Mater. Interfaces*, 2019, **11**, 25790–25795.
- Z. Zeb, Y. C. Huang, L. L. Chen, W. B. Zhou, M. B. Liao, Y. Y. Jiang, H. T. Li, L. M. Wang, L. Wang, H. Wang, T. Wei, D. J. Zang, Z. J. Fan and Y. G. Wei, *Coord. Chem. Rev.*, 2023, **482**, 215058.
- Y. J. Wang, Z. F. Qiu, Y. Zhang, F. F. Wang, Y. Zhao and W. Y. Sun, *Dalton Trans.*, 2024, **53**, 3685–3689.
- A. V. Anyushin, A. Kondinski and T. N. Parac-Vogt, *Chem. Soc. Rev.*, 2020, **49**, 382–432.
- S. S. Wang and G. Y. Yang, *Chem. Rev.*, 2015, **115**, 4893–4962.
- L. X. Cai, S. C. Li, D. N. Yan, L. P. Zhou, F. Guo and Q. F. Sun, *J. Am. Chem. Soc.*, 2018, **140**, 4869–4876.
- M. Samaniyan, M. Mirzaei, R. Khajavian, H. Eshtiagh-Hosseini and C. Streb, *ACS Catal.*, 2019, **9**, 10174–10191.
- J. L. Wang, J. P. Cao, Z. Y. Du, X. M. Liu, J. N. Li, Q. D. Ping, T. T. Zang and Y. Xu, *Chin. Chem. Lett.*, 2023, **34**, 106917.
- Y. H. Zhu, J. B. Yang, P. F. Yan, Z. M. Dong, H. Mei and Y. Xu, *J. Mater. Chem. A*, 2024, **12**, 5340–5347.
- L. Yang, Z. Zhang, C. N. Zhang and X. L. Wang, *Rare Met.*, 2024, **43**, 236–246.
- J. L. Wang, X. M. Liu, Z. Y. Du and Y. Xu, *Dalton Trans.*, 2021, **50**, 7871–7886.
- N. Li, J. Liu, J. J. Liu, L. Z. Dong, Z. F. Xin, Y. L. Teng and Y. Q. Lan, *Angew. Chem., Int. Ed.*, 2019, **58**, 5226–5231.
- N. Li, J. Liu, B. X. Dong and Y. Q. Lan, *Angew. Chem., Int. Ed.*, 2020, **59**, 20779–20793.
- T. J. Wilke and M. A. Barteau, *J. Catal.*, 2020, **382**, 286–294.
- P. F. Yan, X. Y. Li, J. L. Wang, J. H. Pan, H. Xu, Y. H. Zhu, Q. L. Chen, H. Mei and Y. Xu, *Mol. Catal.*, 2024, **561**, 114162.
- Y. H. Zhu, P. F. Yan, L. T. Xu, Z. Y. Du, H. Mei and Y. Xu, *Dalton Trans.*, 2024, **53**, 7257–7262.
- C. L. Wu, X. H. Qiao, C. M. Robertson, S. J. Higgins, C. Cai and R. N. u. A. Vezzoli, *Angew. Chem., Int. Ed.*, 2020, **59**, 12029–12034.
- L. Z. Qiao, M. Song, A. F. Geng and S. Yao, *Chin. Chem. Lett.*, 2019, **30**, 1273–1276.
- Y. Y. Li, A. G. Walsh, D. S. Li, D. Do, H. Ma, C. H. Wang, P. Zhang and X. T. Zhang, *Nanoscale*, 2020, **12**, 17245–17252.
- K. Talbi, F. Penas-Hidalgo, A. L. Robinson, P. Gotico, W. Leibl, P. Mialane, M. Gomez-Mingot, M. Fontecave,

- A. Solé-Daura, C. Mellot-Draznieks and A. Dolbecq, *Appl. Catal., B*, 2024, **345**, 123681.
- 41 X. X. Li, L. Zhang, J. Liu, L. Yuan, T. Wang, J. Y. Wang, L. Z. Dong, K. Huang and Y. Q. Lan, *J. Am. Chem. Soc. Au*, 2021, **1**, 1288–1295.
- 42 M. Cheng, Z. Zhang, H. L. Li and G. Y. Yang, *Inorg. Chem. Commun.*, 2018, **96**, 69–72.
- 43 F. Y. Cui, X. Y. Ma, C. Li, T. Dong, Y. Z. Gao, Z. G. Han, Y. N. Chi and C. W. Hu, *J. Solid State Chem.*, 2010, **183**, 2925–2931.
- 44 D. D. Zhu, J. L. Liu and S. Z. Qiao, *Adv. Mater.*, 2016, **28**, 3423–3452.
- 45 J. D. Hong, W. Zhang, J. Ren and R. Xu, *Anal. Methods*, 2013, **5**, 1073–1356.
- 46 Y. X. Pan, Y. You, S. Xin, Y. Li, G. Fu, Z. Cui, Y. L. Men, F. F. Cao, S. H. Yu and J. B. Goodenough, *J. Am. Chem. Soc.*, 2017, **139**, 4123–4129.
- 47 J. Du, Y. Y. Ma, X. Xin, H. Na, Y. N. Zhao, H. Q. Tan, Z. G. Han, Y. G. Li and Z. H. Kang, *Chem. Eng. J.*, 2020, **398**, 125518.
- 48 J. N. Qin, S. B. Wang and X. C. Wang, *Appl. Catal., B*, 2017, **209**, 476–482.
- 49 T. Maschmeyer and M. Che, *Angew. Chem., Int. Ed.*, 2010, **49**, 1536–1539.
- 50 M. Wang, J. X. Liu, C. M. Guo, X. S. Gao, C. H. Gong, Y. Wang, B. Liu, X. X. Li, G. G. Gurzadyan and L. C. Sun, *J. Mater. Chem. A*, 2018, **6**, 4768–4775.
- 51 W. T. Eckenhoff, *Coord. Chem. Rev.*, 2018, **373**, 295–316.
- 52 V. S. Thoi, N. Kornienko, C. G. Margarit, P. D. Yang and C. J. Chang, *J. Am. Chem. Soc.*, 2013, **135**, 14413–14424.
- 53 C. Gao, S. M. Chen, Y. Wang, J. W. Wang, X. S. Zheng, J. F. Zhu, L. Song, W. K. Zhang and Y. J. Xiong, *Adv. Mater.*, 2018, **30**, 1704624.
- 54 C. M. Gao, H. N. Yu, L. N. Zhang, Y. H. Zhao, J. X. Xie, C. J. Li, K. Cui and J. H. Yu, *Anal. Chem.*, 2020, **92**, 2902–2906.
- 55 S. L. Xie, J. Liu, L. Z. Dong, S. L. Li, Y. Q. Lan and Z. M. Su, *Chem. Sci.*, 2019, **10**, 185–190.
- 56 K. Zhao, S. L. Zhao, C. Gao, J. Qi, H. J. Yin, D. Wei, M. F. Mideksa, X. L. Wang, Y. Gao, Z. Y. Tang and R. B. Yu, *Small*, 2018, **14**, 1800762.
- 57 S. Linic, P. Christopher and D. B. Ingram, *Nat. Mater.*, 2011, **10**, 911–921.
- 58 J. L. Wang, H. Xu, Q. Wang, J. L. Zhou, X. Y. Xiang, S. M. Li, H. Mei and Y. Xu, *Chem. Eng. J.*, 2023, **474**, 145662.